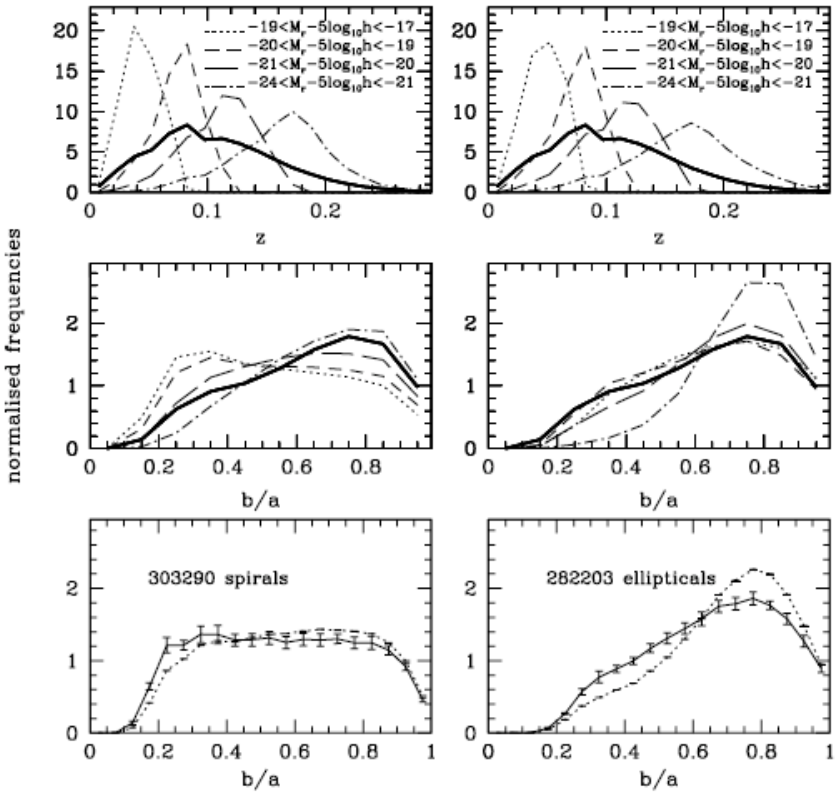

Figure 1. Left panels show distributions obtained for spiral galaxies, right panels for elliptical galaxies. Top panels: distribution of galaxy redshifts, normalised so that the area under each curve is unity. The thick solid line corresponds to all the galaxies in the SDSS-DR6. The thin lines show the distribution of axis ratios for galaxies in different bins of absolute magnitude as indicated in the key, and for spiral and elliptical galaxies separately. Middle panels: normalised distribution of axis ratios for the same samples of galaxies as in the top panels; the thick line corresponds to the full sample of galaxies. Bottom panels: Distribution of axis ratios, summed over all luminosities. The solid lines show the results when a $1/V_{max}$ weight is applied to each galaxy. The dotted lines show the results with no weighting. Errors are calculated using the Jack-knife technique.

Padilla & Strauss 2008, MNRAS, 388, 1321

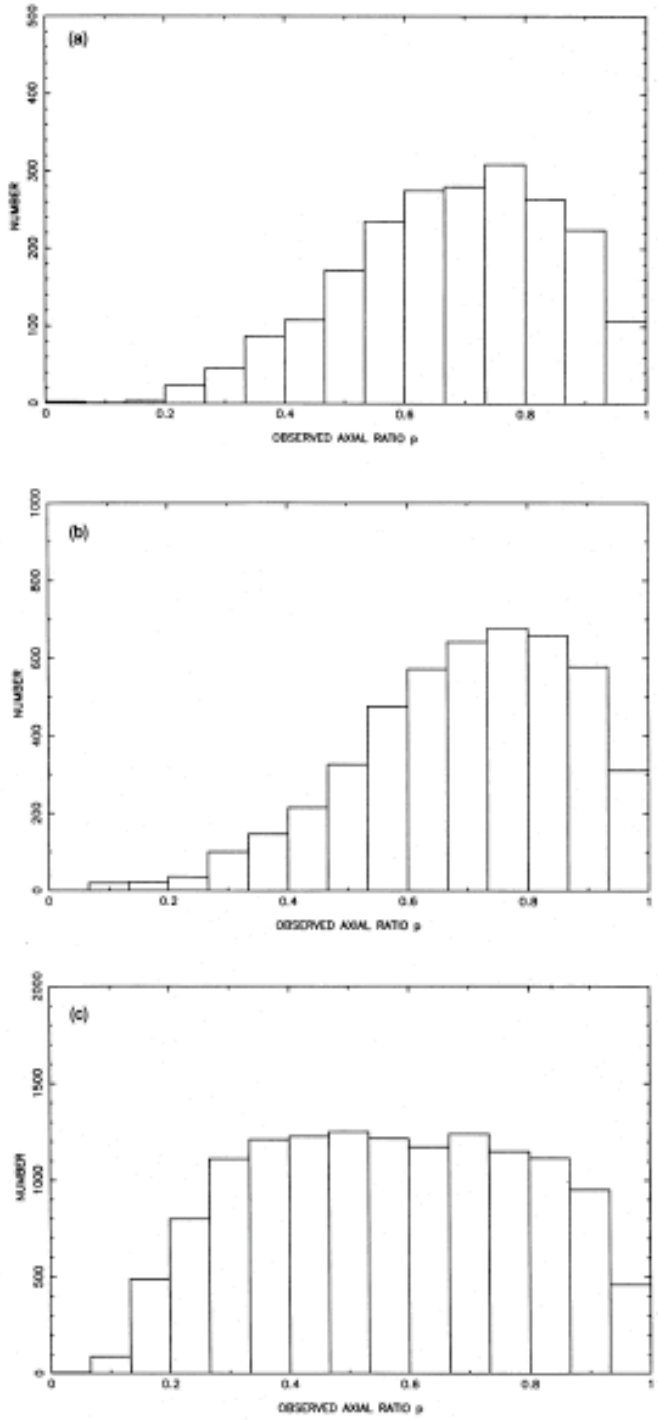

Figure 2. Distribution of observed axial ratios for (a) APM ellipticals, (b) APM S0s and (c) APM spirals. The distribution function $\phi(p)$ is related to the number of galaxies in each bin, so that $N(p_i) = \phi(p_i)\,\Delta p N_{tot}$, as defined in the text.

Lambas et al. 1992, MNRAS, 258, 404

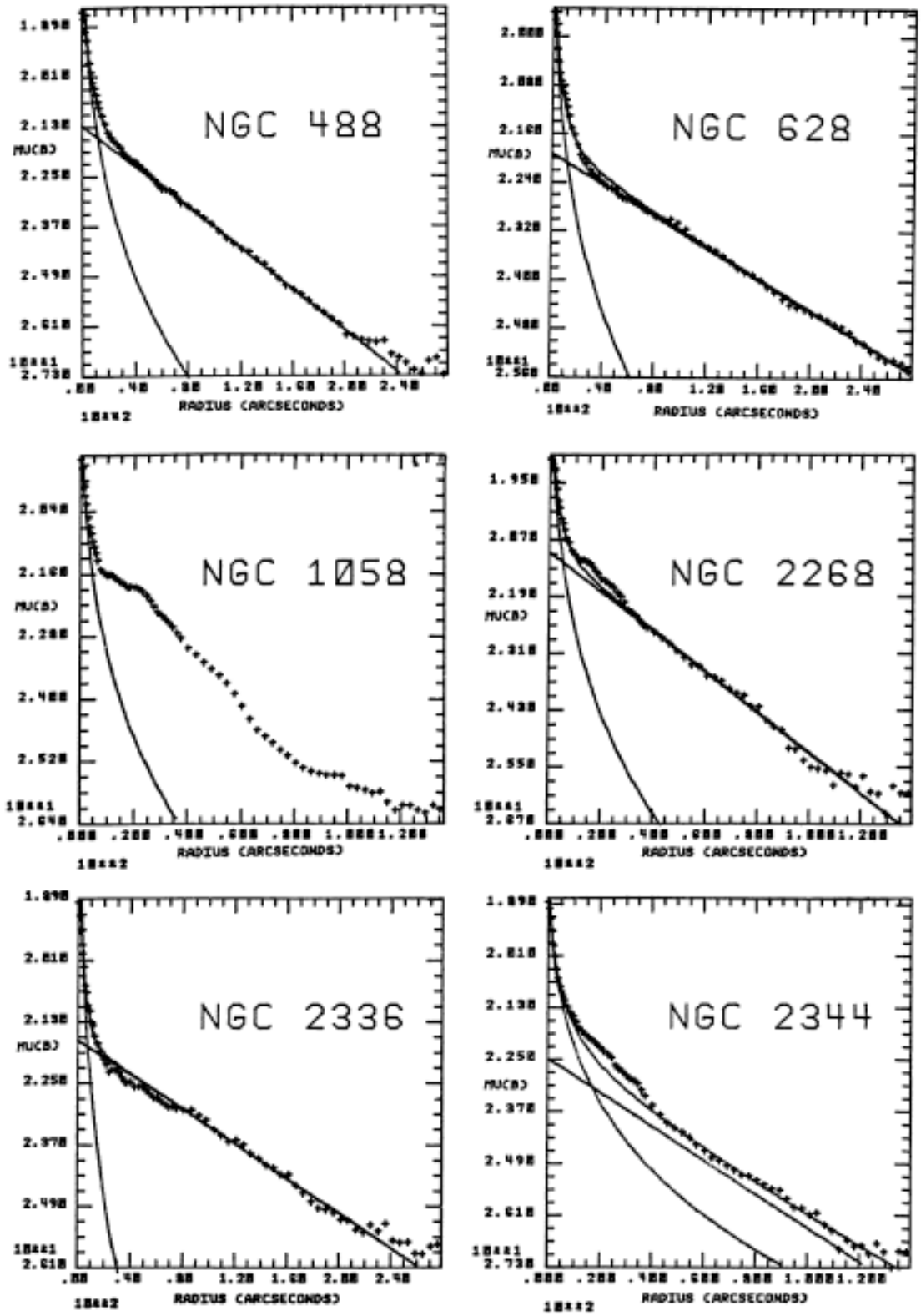

FIG. 6.—Elliptically averaged profiles for the 26 spiral galaxies. For NGC 4594 the north half of the minor axis is shown. Where an iterative decomposition was possible, disk, bulge, and total profiles are shown. In all other cases, only the bulge fit is shown.

Boroson, 1981, ApJS, 46, 177

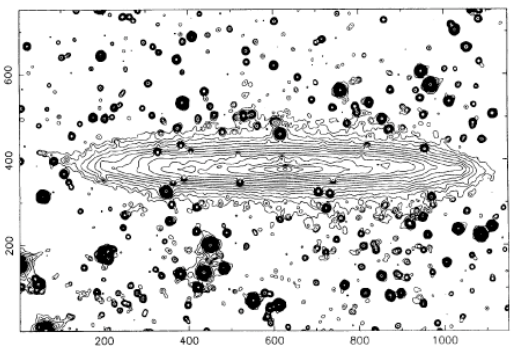

FIG. 2. Contour plot of NGC 5907. Contours are from 17.5 to 26.0 R mag/sq arcsec. One pixel=0.77″, so 100 pixels=4.1 kpc, assuming a distance of 11 Mpc.

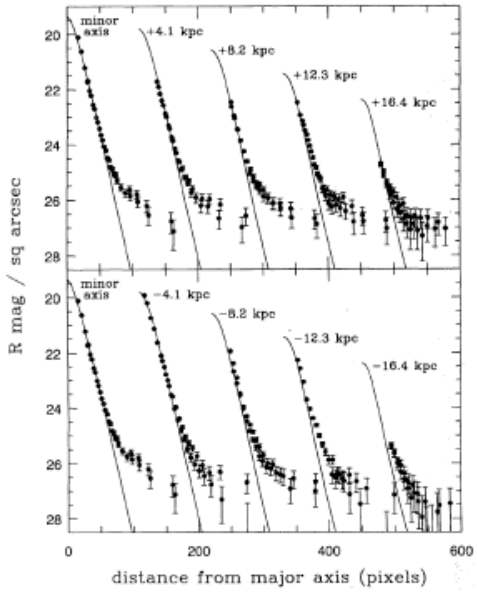

FIG. 6. Profiles parallel to the minor axis, made by binning up rectangular bands 100 pixels wide after masking out dust, foreground stars and background galaxies. Different sides of the galaxy are shown separately, but profiles above and below the major axis were folded about their axis of symmetry and displayed on the same plot. (Note that one pixel is 41 pc, assuming a distance to the galaxy of 11 Mpc.) Also shown (lines) are the predictions of the simple thin disk model with parameters given in Table 2. It can be seen that the brighter portions of the galaxy are extremely well fit with this model, which has h_z constant with R. Deviations from this model are only seen below $R=25$ mag/sq arcsec.

Morrison et al. 1994, AJ, 108, 1191

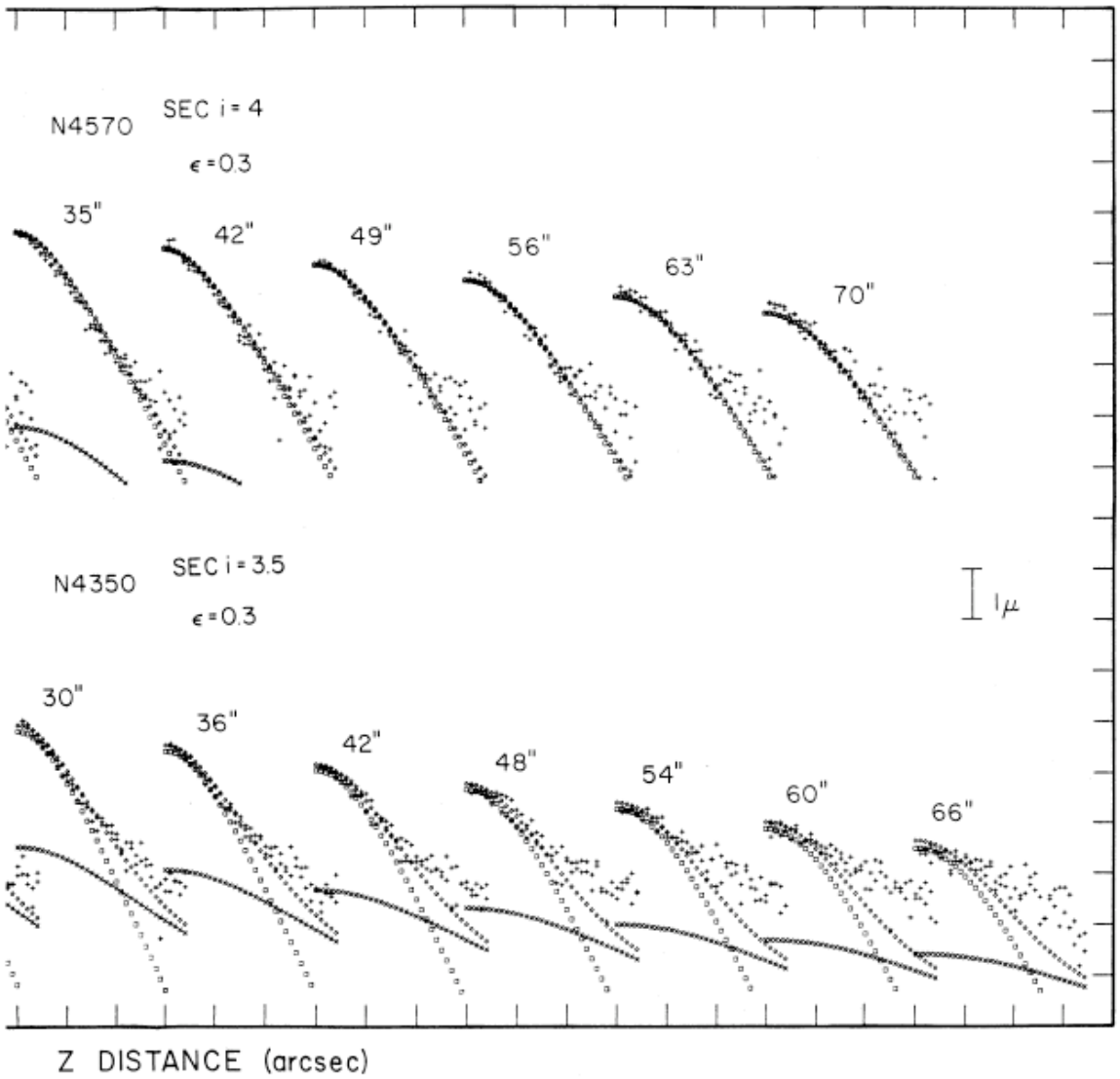

e: *pluses*, one side of the observed PP, both quadrants; *squares*, the model disk PP as computed from eq. (1) and the final alaxy, disk plus bulge, PP. The inclination of NGC 4350 has sec i = 3.5 and the bulge is given as ϵ = 0.3; NGC 4570 has

Burstein 1979, ApJ, 234, 829

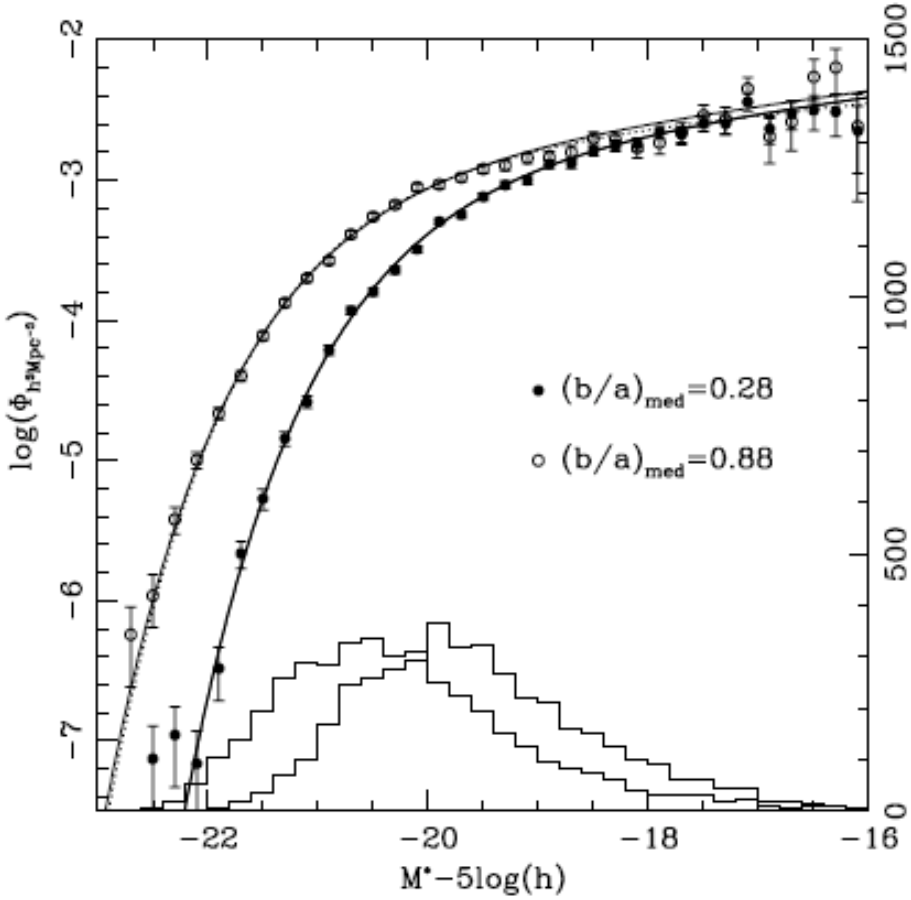

FIG. 4.— The luminosity functions for the nearly face-on subsample (open circles) and the nearly edge-on subsample (solid circles). Smooth curves are the luminosity functions obtained using the STY method. Dotted curves show the best fit of the data points with a Schechter function. Solid curves are the fit results assuming $\alpha = \langle \alpha_{\rm sub} \rangle = -1.25$. Points and errors are obtained from the SWML method. Histograms near the bottom are the numbers of galaxies in bins of absolute magnitude. The results for edge-on galaxies are shifted vertically by a factor of two for easy to compare the shape of LFs.

Shao et al. 2007, ApJ, 659, 1159

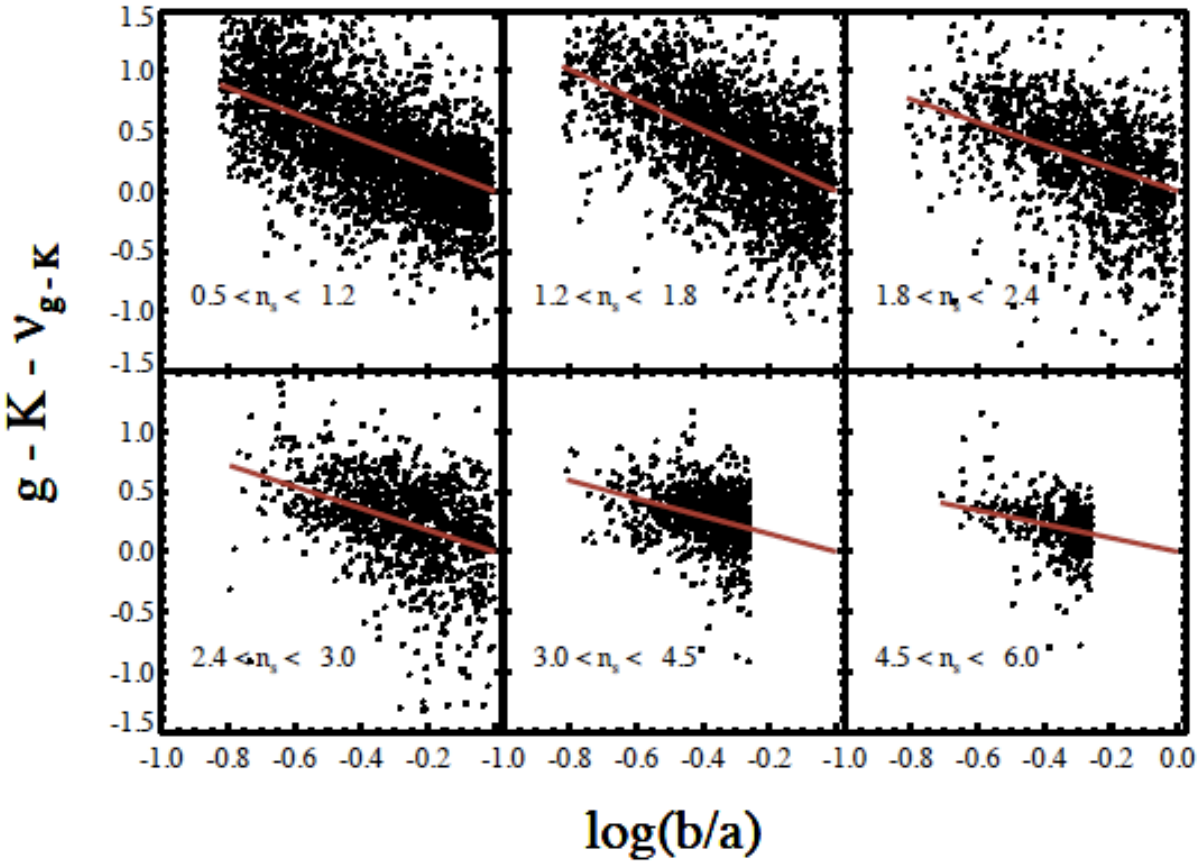

FIG. 5.— The difference between a galaxy's $g-K$ color and the mean value of the $g-K$ color for a face-on galaxy with the same M_K and n_s is shown as a function of axis ratio for six different bins of n_s. We see in all cases, even for the highest n bin, there is a clear trend for more inclined galaxies to be redder. The relationship seems to be linear in $\log b/a$ with a slope that becomes shallower with higher n.

Maller et al. 2009, ApJ, 394, 406

Tully et al. 1998, AJ, 115, 2264

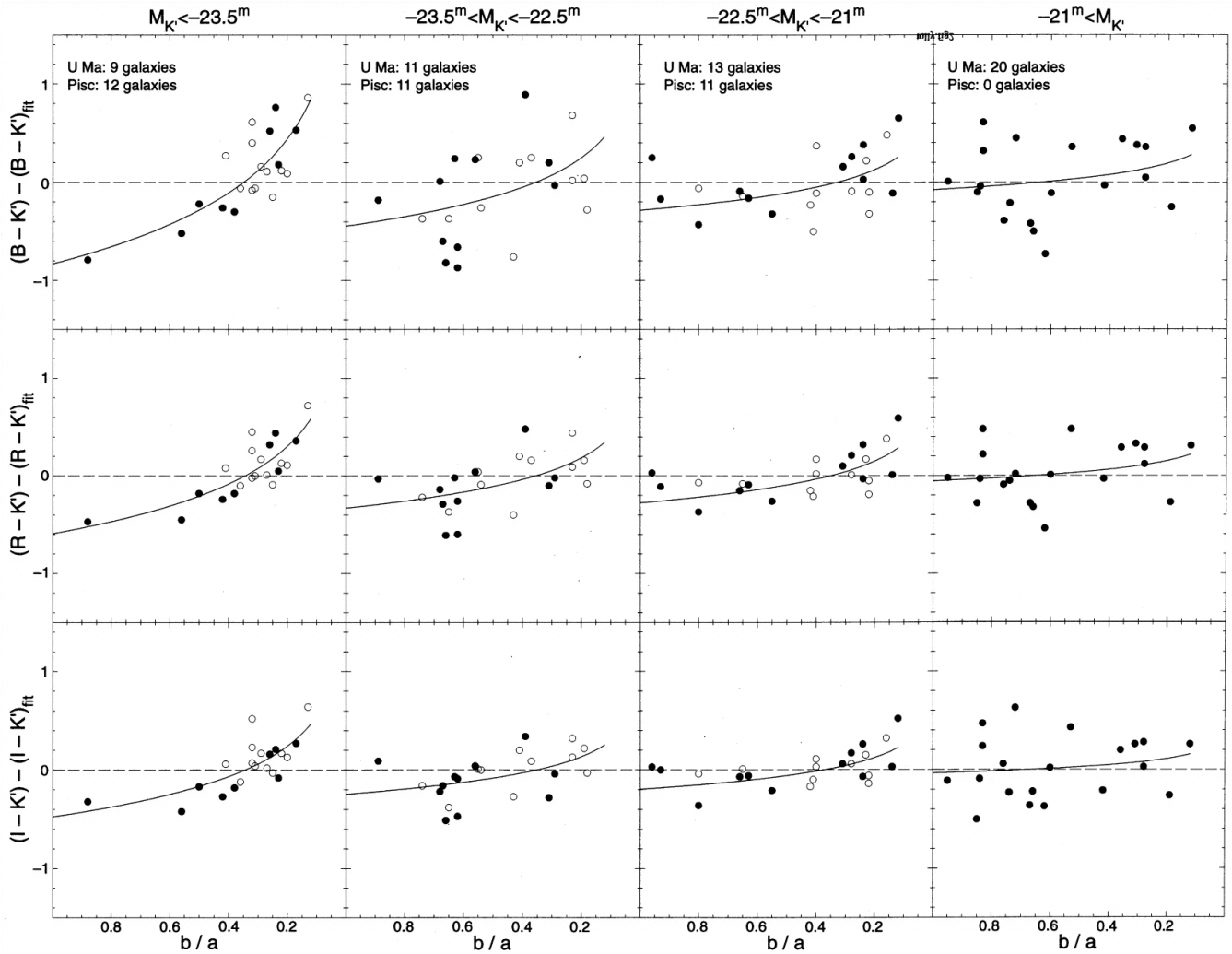

FIG. 2.—Deviations in color from the mean relations of Fig. 1 as a function of axial ratio b/a. The top row of panels illustrates deviations at $B-K'$, the middle row illustrates deviations at $R-K'$, and the bottom row illustrates deviations at $I-K'$. The left column of panels isolates the fraction of the sample with $M_{K'} < -23.5$ mag (nine galaxies in Ursa Major and 12 galaxies in Pisces), the panels second from left show data for galaxies with -23.5 mag $< M_{K'} < -22.5$ mag (11 galaxies in Ursa Major and 11 galaxies in Pisces), the panels second from right show data for galaxies with -22.5 mag $< M_{K'} < -21$ mag (13 galaxies in Ursa Major and 11 galaxies in Pisces), and the right set of panels shows data for galaxies with -21 mag $< M_{K'} < -19.2$ mag (20 galaxies in Ursa Major and none in Pisces). *Filled circles*: Ursa Major; *open circles*: Pisces. The solid line in each panel gives the best fit for the analytic expression $\gamma_\lambda \log(a/b)$ with the requirement that the dependence on b/a be nullified.

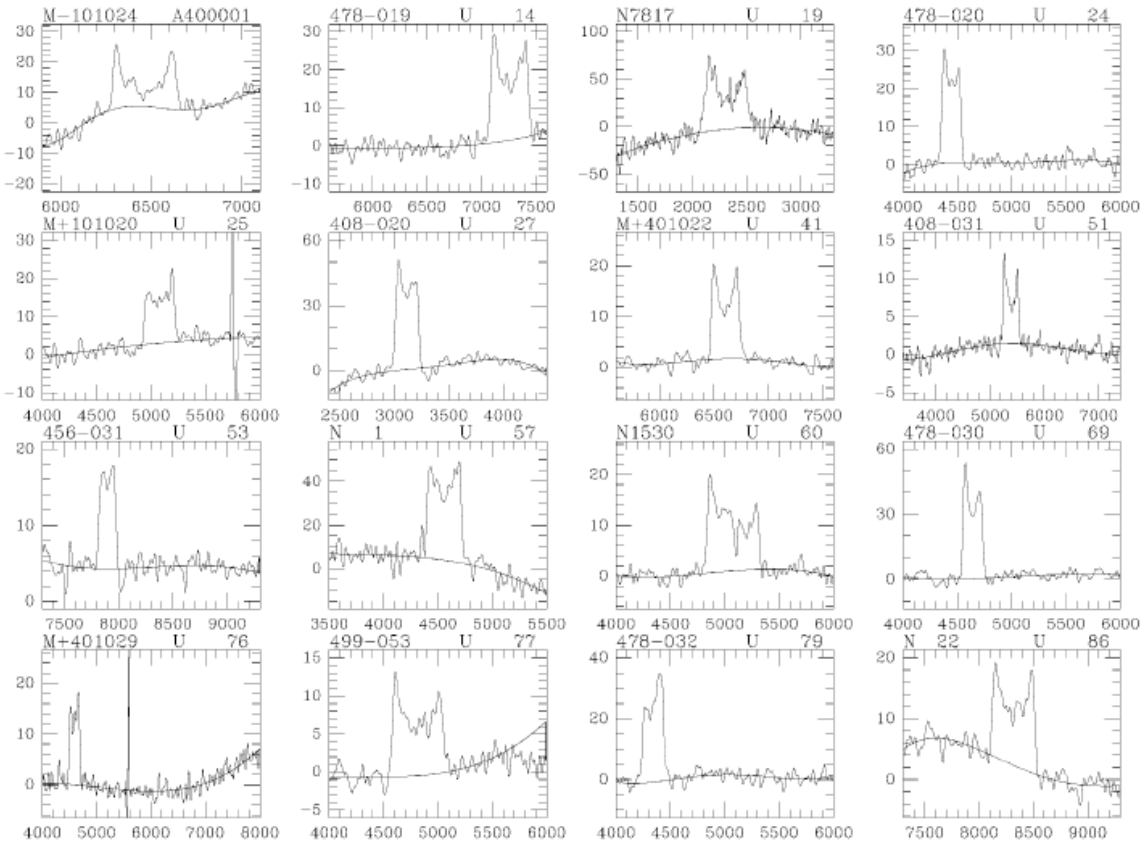

FIG. 1.—A sample montage of spectral profiles for the first 16 galaxies included in Table 1. The x-axis is heliocentric velocity in km s^{-1}; the y-axis is flux in mJy.

Haynes et al. 1999, AJ, 117, 2039

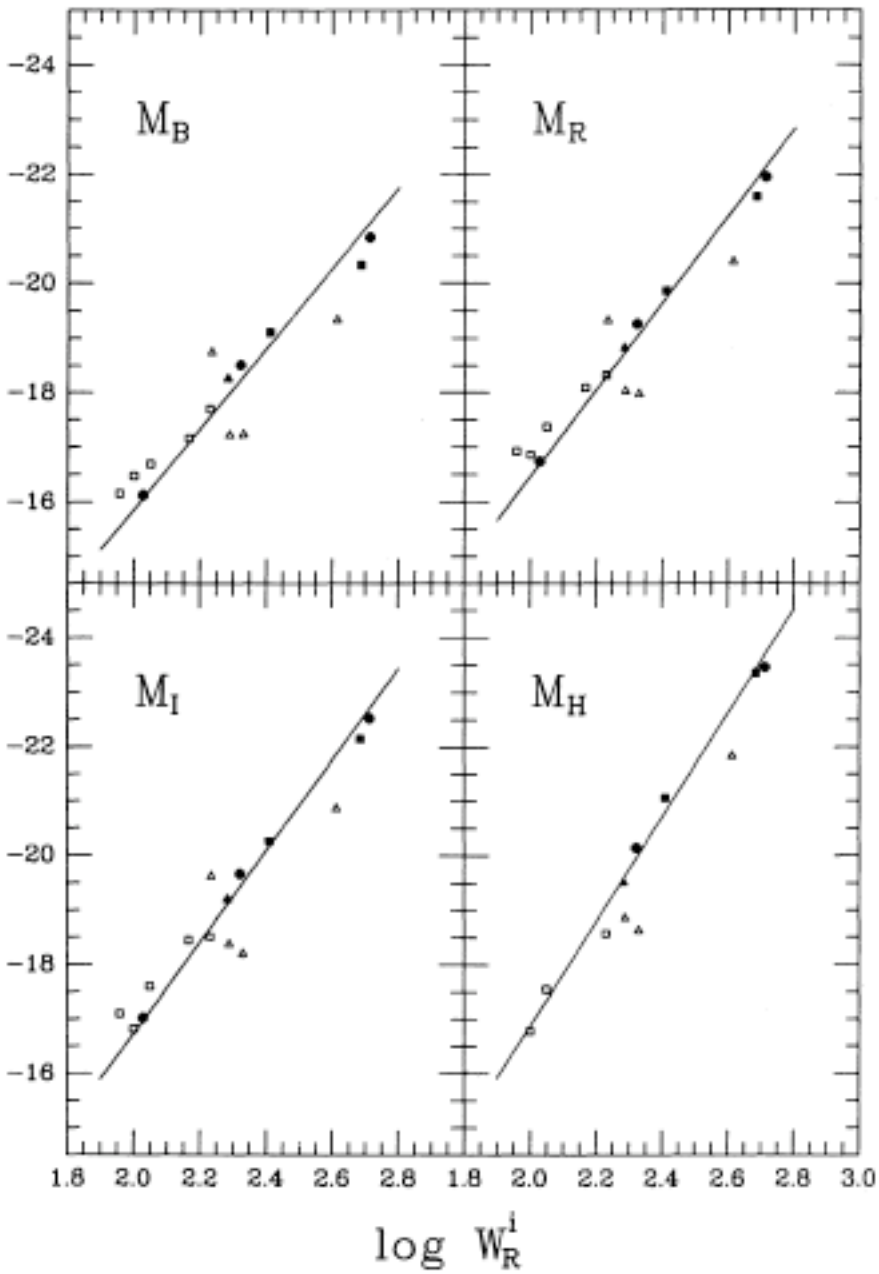

FIG. 1.—The TF relations for the members of the Local (*points*), Sculptor (*triangles*), and M81 (*squares*) groups. The filled symbols represent galaxies with individual distance determinations using Cepheids, RR Lyraes, and/or planetary nebulae. Open symbols represent systems assigned a mean group distance. Note the significant line-of-sight depth for the Sculptor Group. The solid line in each panel is the result of a least-squares fit to similar data for galaxies in the Ursa Major Cluster (Pierce & Tully 1988, 1991) minimizing the residuals in line width. The zero point was established from the six systems with individual distance determinations (i.e., the solid points).

Pierce & Tully 1992, ApJ, 387, 47